Research Square

Preprints are preliminary reports that have not undergone peer review.
They should not be considered conclusive, used to inform clinical practice,
or referenced by the media as validated information.

Cross-kingdom comparative proteomics reveals conserved deployment of T2-ribonucleases during wound responses in plants and animals

Timothy Callum Byatt
University of Bristol
Oscar Peña
University of Bristol
Ashley Pridgeon
University of Bristol
Phil Lewis
University of Bristol
Kate Heesom
University of Bristol
Keara Franklin
University of Bristol
Pierre Buscaill
University of Bristol
Paul Martin
paul.martin@bristol.ac.uk

University of Bristol

Article

Keywords: Wound, Zebrafish, Arabidopsis, Rnaset2, RNS, T2 Ribonuclease

Posted Date: November 2nd, 2026

DOI: https://doi.org/10.21203/rs.3.rs-11321761/v1

License: This work is licensed under a Creative Commons Attribution 4.0 International License. Read Full License

Additional Declarations: Competing interest reported. P.M. is a member of the editorial board for npj Regenerative Medicine. The authors declare no other competing interests.

Abstract

Wound healing is essential to the survival of all living organisms, and yet the molecular components of wound responses are almost always studied in one organism at a time, thus limiting opportunities for discovering conserved pathways and potential novel gene discovery. Here, we developed a reciprocal plant-animal proteomic strategy to discover whether these evolutionarily distant organisms might deploy homologous proteins during their wound response. This approach identified T2 ribonucleases as a conserved wound-responsive protein family between zebrafish and Arabidopsis. Our functional analysis then revealed a previously unrecognised role for zebrafish Rnaset2 in macrophage-mediated clearance of cell debris during wound repair and identified a previously unrecognised role for Arabidopsis RNS1 in regulating wound-triggered antibacterial defence. This study demonstrates how comparative plant and animal wound proteomics can identify understudied, conserved wound-responsive protein families and reveal previously unrecognised functions with potential relevance to tissue repair and crop resistance.

INTRODUCTION

Studies of wound healing in diverse animal model organisms have uncovered many of the fundamental cellular and molecular mechanisms that underpin tissue repair[1–3]. These findings have revealed mechanisms ranging from the migration and remodelling of cells at wound margins to the damage signals that initiate inflammatory responses[4–7]. Comparative studies across animal models and developmental contexts have further shown that differences in wound outcome can reveal mechanisms that are difficult to identify from studies of a single model alone. For example, comparison of skin repair in adult and embryonic mice has highlighted differences in inflammatory responses, growth-factor profiles and tissue mechanics associated with scar formation[8–10], while comparisons of cardiac repair in zebrafish, neonatal mice and adult mice have implicated differences in macrophage responses in the progression towards regeneration or fibrosis[11,12].

Although all organisms have evolved strategies to respond to tissue damage to restore tissue integrity, plants and animals, however, differ profoundly in the physical and cellular mechanisms available for wound repair. In animals, cells at the wound margin can migrate to close the epithelial gap, while motile immune cells are recruited to wounds to restrict infection and coordinate repair. In plants, rigid cell walls constrain cell migration, and so wound repair instead relies on local cellular reprogramming, growth and tissue remodelling[5,13–20].

Recent comparative reviews between plant and animal have highlighted shared features of wound responses across plants and animals, while emphasising substantial differences in their cellular and molecular implementation[21]. Similar comparisons have been made for immune signalling, including parallels between animal cytokines and plant phytocytokines, despite divergence in their molecular processing and release mechanisms[22]. Thus, although plants and animals share fundamental requirements to detect damage, restrict microbial invasion and restore tissue integrity, the molecular mechanisms by which these processes are implemented can be highly divergent.

Despite these profound differences, plants and animals share molecular features of the early response to tissue damage[23]. One immediate parallel is a rapid increase in cytosolic calcium that propagates from

damaged cells to neighbouring cells and is followed by production of reactive oxygen species (ROS), which can act both directly as a microbicidal response and as a signalling mechanism to activate defence responses at the wound site[24,25]. Such parallels raise the possibility that additional molecular components of the wound response may have been conserved despite major divergence in tissue organisation and repair mechanisms.

Rather than assuming conservation from sequence homology alone, we reasoned that proteins that are independently induced by wounding in both an animal and a plant would provide us with candidate components of the wound response. To uncover such components, we undertook a comparative proteomic analysis combined with bioinformatic analyses to identify homologous proteins that were upregulated following wounding in each organism. This approach enriches for conserved wound-responsive components while retaining the possibility of lineage-specific functions.

Here, we compared wound-responsive proteomes from zebrafish and Arabidopsis to identify homologous proteins that are independently induced following tissue damage. This analysis identified T2 ribonucleases as a conserved wound-responsive protein family, prompting functional analysis of the zebrafish Rnaset2 and Arabidopsis RNS1 proteins. We find that Rnaset2 is required for efficient macrophage-associated clearance and timely wound resolution in zebrafish, whereas RNS1 restrains the early wound-associated antibacterial response in Arabidopsis. Together, these findings reveal conservation at the level of wound-responsive molecular components alongside divergence in the biological functions executed by orthologous proteins.

RESULTS

Zebrafish and Arabidopsis exhibit distinct morphological responses to tissue injury

To establish a framework for cross-kingdom comparison of wound responses, we developed and characterised complementary wound models in zebrafish and *Arabidopsis thaliana* (Arabidopsis). Wound samples were collected across the respective healing time courses and analysed by scanning electron microscopy (SEM) and histology (Fig. 1A). Zebrafish larvae rapidly re-epithelialised small needle-stick wounds (Fig. 1B **and C**). SEM revealed that epithelial cells at the wound margins had begun to close over the denuded region within 1 hour post-wounding (hpw), leaving an uneven surface at the former wound site (Fig. 1C). By 24 hpw, the epithelial surface appeared continuous, with little visible evidence of the original wound (Fig. 1C). However, histological sections showed that restoration of the surface epithelium did not coincide with complete restoration of the underlying tissue, which continued to undergo localised remodelling (Fig. 1D).

In contrast, punch wounds in Arabidopsis leaves remained open throughout the observation period, with little apparent reduction in wound size up to 7 days post-wounding (dpw) (Fig. 1E). A narrow chlorotic region developed around the wound site over this period, with persistent morphological changes at the wound margin (Fig. 1E). SEM revealed that cells immediately surrounding the wound appeared deflated relative to cells further from the wound, consistent with localised tissue damage at the wound margin (Fig. 1F). Histological analysis further revealed localised cell-wall reinforcement at the wound perimeter, rather than a widespread structural remodelling across the surrounding tissue (Fig. 1G).

(A) Experimental workflow for wounding and tissue collection from zebrafish and Arabidopsis for Scanning electron microscopy (SEM) and histological analysis. **(B)** SEM of a 6-day-post-fertilisation (dpf) zebrafish larva at 6 hpw. The white box indicates the region shown at higher magnification in (C), and the red dashed line indicates the position of the transverse sections shown in (D). **(C)** Higher-magnification SEM images of zebrafish wounds immediately after wounding (0 hpw) and at 1 hpw. White asterisks indicate the wound centre, and white arrowheads indicate the epithelial wound margins. **(D)** Methylene Blue stained resin sections through flank regions of wounded zebrafish larvae (6 dpf) at 0 and 24 hpw. Black arrowheads indicate epithelial wound margins, and the white asterisk indicates newly formed healing tissue. **(E)** Brightfield images of Arabidopsis leaves before wounding (unwounded) and at 1, 2 and 7 days post-wounding (dpw). **(F)** SEM of an *Arabidopsis* leaf wound at 7 dpw. The boxed region is shown at higher magnification; black arrowheads indicate deflated cells at the wound margin, and white arrowheads indicate healthy cells away from the wound. **(G)** Histological sections of unwounded and wounded Arabidopsis leaves at 7 dpw stained with Safranin O, corresponding to dashed lines in (C) at the wound perimeter (yellow line) and within the wound (red line). **Scale bars**: (B-D) = 1 mm; (C, inset) = 50 μm; (E') = 100 μm; (E'', F) = 50 μm.

Thus, zebrafish and Arabidopsis face the same fundamental challenge of restoring tissue integrity, in response to wounding. We therefore asked whether comparative proteomics could identify conserved molecular components that are deployed during wound responses in these evolutionarily distant organisms, and thereby reveal previously unrecognised components of wound repair in animals and plants.

Reciprocal cross-kingdom proteomics identifies conserved wound-responsive protein families

To identify homologous proteins that are wound-responsive in both plants and animals, we performed a reciprocal cross-kingdom proteomic screen comparing wounded and unwounded zebrafish larvae and Arabidopsis leaves (Fig. 2A). To increase the proportion of wounded tissue relative to unwounded tissue zebrafish larvae received three needle wounds to the flank, and Arabidopsis leaves were subjected to multiple grid-line scratch wounds. Samples were collected before wounding and at 1 and 48 hpw in zebrafish, and at 1 and 24 h post-wounding (hpw) in Arabidopsis. Protein extracts were analysed by tandem mass tag (TMT) mass spectrometry.

(A) Experiment design for comparative proteomic analysis of wound responses in zebrafish and Arabidopsis. Zebrafish and Arabidopsis were sampled before wounding (unwounded) and the indicated times post-wounding (hpw). Proteins were digested with trypsin and analysed by mass spectrometry. **(B)** Differential protein abundance and pathway analysis in wounded zebrafish tissue. Log_2 fold change (log_2FC) in protein abundance versus $-log_{10}(P)$ at 1 and 48 hpw relative to unwounded controls. Vertical dashed lines indicate $log_2FC = -1$ and $+1$; horizontal dashed lines indicate $P = 0.05$. Diseases and Biological Functions identified by Qiagen Ingenuity Pathway Analysis, shown for annotations with bias-corrected *z*-scores ≥ |2|. **(C)** Differential protein abundance and gene set enrichment analysis in wounded Arabidopsis tissue. Log_2FC in protein abundance versus $-log_{10}(P)$ at 1 and 24 hpw relative to unwounded controls. Vertical dashed lines indicate $log_2FC = -1$ and $+1$. Gene ontology (GO) terms enriched among proteins showing altered abundance ($P < 0.05$) at 1 or 24 hpw. **(D)** Reciprocal orthologue analysis of Arabidopsis wound-responsive proteins. Log_2FC in

Arabidopsis (x-axis) is plotted against log_2FC of their zebrafish homologues (y-axis). Highlighted regions indicate conserved increases in protein abundance ($log_2FC \geq 0.6$ and ≥ 1). **(E)** Reciprocal orthologue analysis of zebrafish wound-responsive proteins. Log_2FC in zebrafish (x-axis) is plotted against log_2FC of their Arabidopsis homologues (y-axis). Highlighted regions indicate $log_2FC \geq 0.6$ or ≥ 1 (increased abundance) and ≤ -0.6 or ≤ -1 (decreased abundance).

Wounding resulted in extensive changes in protein abundance in both organisms. In zebrafish, 2,256 proteins showed changes in abundance at 1 hpw and 2,785 at 48 hpw (Fig. 2B). In Arabidopsis, 488 proteins showed significantly altered abundance at 1 hpw, increasing to 1,385 proteins at 24 hpw (Fig. 2C).

We next profiled the early and late wound-response proteins in both organisms. We examined the zebrafish dataset using Qiagen Ingenuity Pathway Analysis after mapping zebrafish proteins to their human orthologues – because the human datasets are more fully annotated and offer greater clinical relevance[26]. The resulting Diseases and Biological Functions annotations showed marked changes in biological processes between the early and late wound responses (Fig. 2B). Early responses encompassed a suppression of cell migration, cytoskeletal rearrangement and endocytic processes, the precise same protein classes which will subsequently be required for wound closure. In contrast, annotations associated with the later wound response reveal a clear shift in the proteome in response to injury, with strong activation of the “skin lesion” protein class, associated with over 1200 proteins in our dataset. At this time, we also see classes of proteomic changes that would typically be associated with cancer, such as “cell proliferation of tumour cell lines”, which may reflect the well-described parallels between wound healing and cancer, and their shared “hallmarks”, including resistance to cell death and sustained proliferative signalling[27,28]. To assess whether the Arabidopsis wound-responsive proteome captured established wound-associated processes, we performed gene set enrichment analysis (GSEA)[29,30]. At 1 hpw, enriched gene ontology (GO) annotations included “response to wounding”, “response to jasmonic acid”, “response to oxygen-containing compound”, and “defence response” (Fig. 2C), consistent with activation of established wound-associated signalling pathways[23,31]. These stress- and defence-associated categories remained enriched at 24 hpw, indicating that substantial changes in the wound-responsive proteome persisted beyond the early response; however, suppression of ROS responses provide evidence of dampened wound signalling at this later timepoint. Together, these analyses indicated that wounding elicited extensive and biologically coherent proteomic responses in both datasets.

We next developed a reciprocal orthologue-based strategy to identify proteins whose wound-associated changes were conserved between zebrafish and Arabidopsis. First, we selected the most strongly altered proteins from each dataset ($|log_2FC| > 1$, $P < 0.05$), and then identified homologues in the reciprocal proteome using BLAST protein sequence similarity. These candidate orthologues were subsequently mapped back onto the corresponding wound proteomes to determine whether their abundance changed in the same direction following wounding (Figs. 2D and 2E). We performed the analysis in both directions to minimise dependence on either proteome as the starting dataset. This approach identified proteins that were both wound-responsive and represented by homologous proteins in the other kingdom. By comparing wound-induced proteomic changes across zebrafish and Arabidopsis, we established a framework for identifying conserved wound-responsive proteins across divergent biological systems.

Among the conserved wound-responsive proteins, thioredoxins and T2 ribonucleases showed prominent increases in abundance at the later wound-response time points (Figs. 2D and 2E). Thioredoxin proteins showed log_2FC values > 2 in zebrafish at 48 hpw and Arabidopsis at 24 hpw. T2 ribonucleases were similarly increased, with zebrafish Rnaset2 and Arabidopsis RNS1 showing log_2FC > 1 at these respective time points. Both protein classes have previously been implicated in stress and tissue responses[32–36], supporting the capacity of this approach to recover biologically relevant wound-responsive proteins. We did not pursue thioredoxin further because its role in zebrafish wound repair has previously been characterised, including a role in regulating oxidative-burst-dependent neutrophil recruitment[34]. We therefore focused on the T2 ribonucleases Rnaset2 and RNS1. Although zebrafish and Arabidopsis are evolutionarily distant, Rnaset2 and RNS1 showed substantial sequence similarity and conserved predicted structural features (**S1 Fig**).

The reciprocal screen therefore identified Rnaset2 as a candidate wound-responsive regulator in zebrafish. We therefore selected this protein for functional analysis in zebrafish. We also further investigated RNS1 in Arabidopsis to determine whether it has an additional function in the wound response.

Rnaset2 promotes resolution of macrophage-associated wound debris clearance in zebrafish

We next investigated whether the wound-associated proteins identified in our proteomic analysis have functions during wound repair in zebrafish. We focused on Rnaset2 because, although its roles have been described in other contexts including RNA metabolism, neuro-developmental disorders and muscle stem cell fusion [37–41], its function during vertebrate wound repair has not previously been investigated. We then first examined *rnaset2* expression across an extended time course following wounding. *rnaset2* transcript abundance increased more than twofold at 24 h post-wounding (hpw) (Fig. 3A), preceding the increase in Rnaset2 protein abundance detected at 48 hpw in our proteomic dataset.

We next examined the spatial expression of *rnaset2* following wounding using wholemount *in situ* hybridisation. Increased *rnaset2* expression was detected in individual cells with a stellate morphology that were visible surrounding the wound at 24 hpw (Fig. 3B), consistent with an immune-cell population. Previous single-cell RNA-sequencing data have also reported enrichment of *rnaset2* transcripts in zebrafish macrophages[42].

(A) Experimental timeline for wounding and subsequent qRT-PCR and wholemount *in situ* hybridisation (WISH) analyses. qRT-PCR show increased *rnaset2* expression at 24 h post-wounding (hpw). **(B)** Wound-associated expression of *rnaset2* detected by DIG-labelled WISH in 3 dpf zebrafish larvae at 24 hpw. Higher-magnification image shows *rnaset2* expression surrounding an individual wound. **(C)** Multi-channel confocal brightfield images of the flank region of 24 hours post wounding 3 dpf *Tg(mpeg:Gal4FF); Tg(UAS:NfsB-mCherry)* transgenic zebrafish larva. Macrophages were visualised by anti-RFP immunostaining (magenta), and *rnaset2* transcripts were detected by fluorescent *in situ* hybridisation using a Cy5-conjugated tyramide signal amplification system (cyan). Higher magnification view denoted by black inset. White arrowheads indicate expression of *rnaset2* in macrophages. **(D)** SEM time course of wound closure in 6 dpf WT and *rnaset2*^{sh532} mutant (KO) larvae at 0 and 48 hpw. Low-magnification images show the wounded flank. White arrowheads

indicate the wound site. **(E)** Delayed clearance of apoptosis in *rnaset2*^{sh532} mutant wounds. TUNEL staining of WT and *rnaset2*^{sh532} KO larvae at the indicated times following wounding. Double-stranded DNA breaks are shown in cyan and macrophages in magenta. White dashed boxes indicate representative wound regions; boxed regions are shown at higher magnification. **(F)** Quantification of TUNEL staining in the wound region at each timepoint. Each point represents data from a single larva and the point colour indicates genotype (Red = WT, Blue = KO). Mean values (black square) are plotted with 95% confidence intervals. Data were analysed using unpaired two-sided Mann-Whitney tests. Specimen numbers are n = 16 (WT) and 16 (KO) for unwounded; 9 (WT) and 16 (KO) at 6 hpw; 18 (WT) and 18 (KO) at 24 hpw; 35 (WT) and 32 (KO) at 48 hpw; and 32 (WT) and 38 (KO) at 72 hpw. **(G)** More persistent and more swollen macrophages in *rnaset2*^{sh532} mutant wounds. Time-lapse imaging of macrophages at wound sites in 5 dpf WT and *rnaset2*^{sh532} KO larvae. Yellow region outlines the wounded somite, and pink boxes indicate the region of high magnification images. Cyan arrowheads indicate large inclusions within macrophages. Magenta outline indicates macrophage margins. Red arrow indicates direction of macrophage migration. **(H)** More abundant and swollen lysosomes in *rnaset2*^{sh532} mutant wounds. Multi-channel confocal time lapse images of WT and *rnaset2*^{sh532} KO larvae expressing the macrophage reporter Tg(*mpeg1:mCherryCAAX*) were stained with LysoTracker Green DND-20 to reveal lysosomes (yellow). White arrowheads indicate indicate LysoTracker-positive compartments within macrophages. **(I)** Increased accumulation of late-stage autophagic compartments of macrophages in *rnaset2*^{sh532} mutant zebrafish. Transmission Electron Microscopy (TEM) of transverse sections through the wound region in WT and *rnaset2*^{sh532} KO larvae at 24 hpw. Higher-magnification images corresponding to boxed regions are false coloured to indicate lysosomes (blue), autophagosomes (orange), autolysosomes (green). **(J)** Quantification of the size and number of lysosomes, autophagosomes and autolysosomes in the wound region of WT and *rnaset2*^{sh532} KO larvae. Scale bars: B, C, D, E and G, 100 μm; C inset, 20 μm; E inset, 50 μm; G inset, 25 μm; H, 5 μm.

To determine whether wound-associated *rnaset2* expression occurred in macrophages, we performed fluorescent *in situ* hybridisation in wounded zebrafish larvae with fluorescently labelled macrophages. *rnaset2* transcripts were detected predominantly within macrophages at the wound site (Fig. 3C), identifying macrophages as a major cellular source of wound-induced *rnaset2* expression.

We next investigated the consequences of loss of *rnaset2* on wound repair using the *rnaset2*^{sh532} mutant[40]. SEM imaging revealed broadly similar wound closure between WT and mutant larvae, although wound resolution appeared delayed in the *rnaset2*^{sh532} mutants (Fig. 3D). At 6 hpw, mutant wounds exhibited a more pronounced epithelial pucker, while at 24 hpw the wound surface appeared largely resolved in both genotypes, but a residual underlying mound remained in the mutants (Fig. 3D). These observations suggested that loss of *rnaset2* affects the resolution of the wound-associated tissue response rather than preventing initial wound closure.

Since Rnaset2 has previously been implicated in the clearance of apoptotic material by zebrafish microglia in the developing brain[39,40], we next investigated whether loss of *rnaset2* similarly affected cell-debris clearance during wound repair using a terminal deoxynucleotidyl transferase dUTP nick-end labelling (TUNEL) assay to reveal apoptotic cells. TUNEL staining revealed no significant difference between WT and mutant larvae in the absence of wounding or at 24 hpw (P = 0.31 and 0.19, respectively). However, at 48 hpw, TUNEL-positive

signal was significantly increased in mutant wound regions compared with WT (P = 0.018), before returning towards WT levels at 72 hpw (Figs. 3E and 3F). The increased signal was associated with macrophages, suggesting impaired degradation of phagocytosed apoptotic material.

Time-lapse movies using *Tg(mfap4:tdTomato)* fish with fluorescent macrophages, further revealed a striking difference in macrophage morphology and behaviour following wounding. Whereas WT macrophages progressively cleared the wound region, macrophages in *rnaset2*^{sh532} mutants accumulated large intracellular inclusions and became increasingly engorged while continuing to interact with wound-associated material (Fig. 3G and S1 **Movie**). Mutant macrophages also showed reduced motility and delayed resolution from the wound site (Fig. 3G and S1 **Movie**). Together these observations suggest that loss of Rnaset2 impairs the intracellular processing of material phagocytosed during wound clearance.

We therefore examined acidic intracellular compartments using LysoTracker. *rnaset2* mutant larvae displayed enlarged LysoTracker-positive compartments, including within macrophages at wound sites (Fig. 3H; S2 **Movie**), consistent with an accumulation of acidic vesicular compartments. To examine these compartments at ultrastructural resolution, we performed TEM of wound regions at 24 hpw. Mutant wounds contained enlarged macrophages and prominent intracellular vesicular structures (Fig. 3I). Quantification revealed fewer free lysosomes together with increased numbers and sizes of autophagosomes and autolysosomes in mutant wound tissue (Fig. 3J). These changes are consistent with altered lysosomal/autophagic compartment dynamics and provide a potential cellular basis for the accumulation of intracellular material and delayed resolution of wound-associated macrophages in *rnaset2*^{sh532} mutants.

RNS1 negatively regulates wound-triggered antibacterial defence in Arabidopsis

Arabidopsis encodes five T2 ribonucleases (RNS1-RNS5), of which RNS1–RNS3 are the best-characterised members[43]. In our proteomic analysis, RNS1 was the only T2 ribonuclease showing a significant increase in abundance following wounding, whereas RNS2 was the predominant T2 ribonuclease under basal conditions (Figs. 2C and 2E), consistent with their previously described wound-induced and intracellular RNA-turnover functions, respectively[44,45]. We therefore compared Arabidopsis T-DNA insertion mutants in RNS1 (*rns1*; SALK_087165C), and RNS2 (*rns2*; SALK_069588C), to determine whether wound-associated phenotypes were specific to RNS1 or reflected a broader requirement for T2 ribonuclease activity.

Reactive oxygen species (ROS) are among the earliest signals produced following mechanical injury and contribute to wound signalling and antibacterial defence[46,47]. To monitor wound-induced ROS-associated redox changes *in vivo*, we used H_2DCFDA and performed time-lapse fluorescence imaging following wounding. Rapid ROS accumulation was observed at the wound site and subsequently propagated into surrounding tissue in WT, *rns1* and *rns2* plants (Fig. 4A and S3 **Movie**). Notably, *rns1* plants showed detectable ROS accumulation within 30 s of wounding, preceding the response observed in WT and *rns2* plants (Fig. 4A and S3 **Movie**), indicating that loss of RNS1 accelerates the early wound-induced oxidative burst.

(A) Wound-induced oxidative response is accelerated in *rns1* mutants. WT, *rns1* and *rns2* plants were fumigated with 50 µM H_2DCFDA and leaves were mechanically wounded before time-lapse fluorescence

imaging. Oxidative response was monitored at the wound site before wounding (unwounded) and at 30 s, 3 min and 10 min post-wounding. **(B)** Experimental procedure for the electrolyte leakage assays. Leaf discs from WT, *rns1* and *rns2* plants were generated by mechanical punching. Electrolyte leakage was monitored by conductivity over time either directly after punching (C) or after vacuum infiltration with 10^8 CFU mL^{-1} *Xcc*Race6 or water (Mock) (D). **(C)** Wound-associated electrolyte leakage is reduced in *rns1* and *rns2* mutants. Error bars indicate mean ± SE of n = 3 biological replicates. **(D)** Infection-associated electrolyte leakage is increased in *rns1* mutants. Error bars indicate mean ± SE of n = 3 biological replicates. **(E)** Experimental procedure for monitoring bacterial colonization. WT, *rns1* and *rns2* leaves were wounded and inoculated with 10^9 CFU mL^{-1} GFP-expressing *Xcc*Race6. Bacterial colonization was visualized by fluorescence microscopy over time. **(F)** Early wound colonisation by *Xcc*Race6 is reduced in *rns1* mutants. Bacterial colonization was quantified by fluorescence intensity and colonized area. Shaded regions indicate mean ± SE. Specimen numbers are n = 4 (WT) and 4 (*rns1*) for 0 dpi; 6 (WT) and 4 (*rns1*) at 1 dpi; 20 (WT) and 4 (*rns1*) at 3 dpi; 8 (WT) and 4 (*rns1*) at 4 dpi; and 12 (WT) and 12 (*rns1*) at 5 dpi, 4 (WT) and 4 (*rns1*) at 6 dpi, 6 (WT) and 4 (*rns1*) at 7 dpi, 4 (WT) and 4 (*rns1*) at 9 dpi. Unpaired two-sided Mann-Whitney-test was used to determine *P* values, *P < 0.05, **P < 0.01. Scale Bars: A and E = 1 mm

We next assessed wound-associated membrane damage by measuring electrolyte leakage from leaf discs generated by mechanical punching (Fig. 4B). Both *rns1* and *rns2* leaf discs showed lower conductivity than WT over the 7-day observation period (Fig. 4C), indicating reduced wound-associated electrolyte leakage in both mutants.

We next asked whether altered wound responses in *rns1* and *rns2* plants affected antibacterial defence. Leaves were inoculated with *Xanthomonas campestris* pv. *campestris* race 6 (*Xcc*Race6), and infection-associated electrolyte leakage was monitored (Fig. 4B). In contrast to the reduced leakage observed following mechanical wounding alone, *rns1* mutants exhibited greater electrolyte leakage following *Xcc*Race6 infection than WT and *rns2* plants (Fig. 4D), indicating increased infection-associated loss of membrane integrity in the *rns1* mutant.

Finally, we tested whether this altered response in *rns1* was associated with bacterial colonisation of wound sites. Wounds were inoculated with GFP-expressing *Xcc*Race6 and bacterial colonisation was quantified over time by fluorescence microscopy (Fig. 4E). *rns1* mutants showed significantly reduced bacterial colonisation at early time points, with significantly smaller colonised areas at 3 and 4 dpi compared with WT and *rns2* (Fig. 4F), highlighting a specific role for RNS1 in regulating the wound-associated response to bacterial infection. Colonisation subsequently converged between genotypes, indicating that loss of RNS1 restricts early *Xcc* colonisation.

Together, these results indicate that RNS1 negatively regulates wound-triggered antibacterial defence, with loss of RNS1 associated with an accelerated wound-induced oxidative response and restricted early *Xcc* wound colonisation.

DISCUSSION

Wound repair is essential for survival across the tree of life. Here, we demonstrated that T2 ribonucleases are a wound-responsive protein family whose induction is conserved between zebrafish and Arabidopsis.

Functional analysis of the respective family members, Rnaset2 and RNS1, revealed a previously unrecognised role for Rnaset2 in macrophage-mediated clearance during zebrafish wound repair and for RNS1 in restraining early wound-triggered antibacterial defence in Arabidopsis.

The comparative approach used here provides a complementary strategy for identifying components of tissue-damage responses that may be difficult to recognise from studies of individual organisms alone. Although the physical mechanisms of wound repair differ substantially between plants and animals, both systems generate complex molecular responses involving changes in protein abundance, cellular signalling, stress responses and immune activity[23]. Rather than inferring conservation from sequence homology alone, our approach required candidate proteins to be independently wound-responsive, and represented by homologous proteins in both proteomes. This dual requirement enriches for conserved components of the wound response over lineage-specific responses. Among the small number of proteins meeting these criteria, T2 ribonucleases stood out for their consistent late induction in both organisms, despite the evolutionary distance separating zebrafish and Arabidopsis.

We demonstrated that Rnaset2 is required for macrophages to process phagocytosed material efficiently during wound clearance. These observations extend a previously described role for Rnaset2 in clearance of apoptotic material during brain development to a wound-repair context[39,40]. Outside plants, a role for an RNASET2 orthologue in wound-associated innate immunity has previously been reported in the invertebrate medicinal leech, *Hirudo verbana*, where granulocyte-released *Hv*RNASET2 recruits macrophages and shows direct antibacterial activity[48]. Additionally, macrophage-secreted Rnaset2 has been shown to support muscle stem cell fusion [41]. Our study extends these investigations to a vertebrate wound-repair model, and identifies a distinct, cell-intrinsic function for Rnaset2 within the macrophage itself, in the processing of phagocytosed wound debris, rather than as a secreted antimicrobial or chemoattractant signal.

Mechanistically, our findings raise the possibility that Rnaset2 contributes to macrophage function at wounds through the processing of RNA encountered during phagocytic clearance. Extracellular RNA is increasingly recognised as an immune-activating signal that alerts phagocytes to tissue damage and pathogen invasion[49,50], and within the endolysosomal compartment, RNase T2 enzymes process long, structured single-stranded RNA into fragments detectable by nucleic-acid-sensing receptors[38,51,52]. RNase T2 has also recently been shown to restrain TLR13 activation thereby dampening erroneous inflammatory activation[53]. Whether Rnaset2 similarly regulates innate immune receptor signalling, or instead primarily supports housekeeping degradation of phagocytosed material, within wound-associated macrophages are questions raised directly by our findings that will be important to address in future work.

Following injury to animal tissues, a critical step for the restoration of tissue homeostasis is the resolution of inflammation. As we describe above, macrophages appear to resolve more slowly from *rnaset2* ^{sh532} mutant fish, presumably in part because of their incapacity to efficiently digest apoptotic corpses. Engulfment of apoptotic/spent neutrophils at the wound site is well established as a cue for reprogramming macrophages from pro-inflammatory to an anti-inflammatory state[54], and failure of neutrophil clearance at the wound site can contribute to chronic inflammation which is characteristic of many pathologies including chronic non-healing wounds[55]. In light of this, loss of Rnaset2 as investigated here, may have further downstream

consequences for macrophage function. For example, early in wound repair, macrophages displace anti-angiogenic neutrophils and then supply trophic signals to trigger vessel sprouting and subsequently change their phenotypes to regulate the “pruning” of these blood vessels, promoting endothelial cell apoptosis which they subsequently digest[56]. Further studies might usefully investigate whether Rnaset2 deficiency results in dynamic changes in macrophage phenotype and consequently altered wound angiogenesis response and/or its later resolution.

Although Rnaset2 and RNS1 are structurally conserved and both increase in abundance after wounding, our results also show that their downstream biological roles have diverged. Most animal genomes, including zebrafish, utilise a single RNASET2 gene (mouse being a notable exception, which has two), whereas Arabidopsis encodes five T2 ribonuclease paralogues (RNS1-RNS5)[43]. Such lineage-specific expansions are thought to facilitate the evolution of new, often lineage-restricted functions through paralogue specialisation[57–60]. Indeed, RNS3 has been implicated in developmentally regulated programmed cell death during leaf and floral organ senescence[61], illustrating functional diversification within the plant T2 ribonuclease family. Our data are consistent with a model in which the plant T2 ribonuclease family has diversified to support additional roles, which may not be required, or are performed differently, in animal lineages that retain a single family member.

Our proteomic screen identified RNS1, but not RNS2, RNS3, RNS4 or RNS5, as significantly increased in abundance after wounding, consistent with previous reports that RNS1 is specifically wound-inducible whereas RNS2 instead performs a constitutive, intracellular role in ribosomal RNA turnover[44,45]. Wound-induced upregulation of RNS1 has previously been inferred from increases in RNS1 transcript abundance and in RNase activity at a molecular weight consistent with RNS1[35,62], and RNS1 protein itself has been detected proteomically in the context of extracellular-ATP- and mycotoxin-induced stress[36], but our proteomic analysis provides direct protein-level evidence that RNS1 accumulates following wounding. Wound-inducibility of RNase T2 enzymes is not restricted to Arabidopsis. In *Phaseolus vulgaris* (Common Bean), mechanical wounding similarly triggers rapid induction of the RNase T2 homologue *Pv*RNS2[63], suggesting that wound-responsive induction of plant RNase T2 proteins may be broadly conserved across plant species.

Our functional analysis identifies a previously unrecognised role for RNS1 in regulating wound-triggered antibacterial defence. Loss of *RNS1*, but not *RNS2*, accelerated the wound-induced oxidative response and restricted early colonisation of wound sites by *Xcc*Race6. The subsequent convergence in bacterial colonisation further suggests that RNS1 influences the early dynamics of the response rather than determining the eventual outcome of infection. We therefore interpret RNS1 as a negative regulator of the early wound-associated antibacterial response. To our knowledge, no previous study has directly tested a role for RNS-family ribonucleases in plant wound-triggered antibacterial immunity. This phenotype was specific to RNS1 rather than a general consequence of disrupting T2 ribonuclease activity, since *rns2* mutants did not phenocopy *rns1* in the infection assays, despite showing a comparable reduction in wound-associated electrolyte leakage after mechanical injury alone. This specificity is consistent with the distinct subcellular localisations reported for the two proteins. RNS1 is secreted to the extracellular space, whereas RNS2 is retained intracellularly within the ER/vacuolar system[44,45], making RNS1, unlike RNS2, a plausible candidate for acting on extracellular substrates at the wound-pathogen interface.

Our data indicate that RNS1 limits wound-associated defence, potentially acting similarly to other regulators that restrain the induction of costly defence responses[47,64,65]. Consistent with this interpretation, RNS1 was reported to negatively influence stress-associated cell death[36]. Our findings therefore extend the known role of RNS1 in stress responses to the regulation of the early antibacterial response of wounded tissue. The molecular basis of this regulation remains to be determined, but our results raise at least two, non-mutually exclusive hypotheses. First, RNS1 may degrade extracellular RNA released from damaged plant cells that would otherwise act as a damage-associated molecular pattern amplifying wound-associated signalling. Second, RNS1 may degrade microbial RNA at the wound site, altering its availability as a pathogen-associated molecular pattern for recognition by the plant immune system. Distinguishing between these possibilities will require identifying the physiological substrates of RNS1 at wounded, infected leaf surfaces.

Beyond the role identified here, the T2 ribonuclease family has also been implicated in the biogenesis of tRNA-derived small RNAs (tsRNAs), an emerging class of regulatory non-coding RNAs implicated in stress responses across all three domains of life[66]. In Arabidopsis, RNS1 and RNS3 are the principal endoribonucleases generating tsRNAs in siliques, while RNS2 predominates in leaves under normal growing conditions[43], and related activities have been described for RNase T2 homologues in yeast and humans, suggesting that tsRNA production is an evolutionarily conserved feature of this enzyme family[43]. T2 ribonucleases are also induced during phosphate starvation in plants, where they are thought to help recycle phosphate from nucleic acids[67,68]. Whether wound-induced RNS1 similarly contributes to tsRNA biogenesis or nucleotide recycling at wound sites is an interesting question for future study.

Our proteomic datasets also revealed a broader shift in the wound-response proteome over time, with evidence of dampened wound-associated signalling at later time points in both zebrafish and Arabidopsis. This temporal attenuation may reflect mechanisms that limit the duration or magnitude of wound responses, preventing prolonged activation that could otherwise disrupt normal growth or tissue homeostasis[64,69]. Rnaset2 and RNS1 may represent specific examples of this broader phenomenon, and our datasets provide a resource for identifying additional components of these dampening mechanisms in both organisms.

Collectively, these data indicate that reciprocal, proteomics-based comparison of plant and animal wound responses can identify understudied, evolutionarily conserved protein families and reveal biological functions with no obvious precedent in either kingdom individually. This comparative framework provides a route to identifying additional conserved components of wound responses across evolutionary distance, with potential relevance to tissue repair in the clinic and to disease resistance and wound management in agriculture.

MATERIALS AND METHODS

Biological materials and growth conditions

Arabidopsis lines used in this study were in the Columbia 0 (Col-0) background. Plants were grown in a 3:1 mixture of all-purpose compost (Sinclair) and silver sand (Melcourt). Growth conditions were 70% relative humidity under short day conditions with 10 h photoperiods of 120 µmol m^{-2} s^{-1} white light and day/night temperatures of 22°C/20°C in a Snjider Labs Micro Clima-Series High Specs Plant Growth Chamber. Accession numbers and sequence data can be found in the TAIR website and in the Arabidopsis Genome

Initiative or GenBank/EMBL databases under the following accession numbers: RNS1, At2g02990; RNS2, At2g39780; RNS3, At1g26820; RNS4, At1g14210; RNS5, At1g14220. T-DNA insertion mutants were obtained from Nottingham Arabidopsis Stock Centre (NASC): *rns1* (SALK_087165C) and *rns2* (SALK_069588C).

All the experiments with zebrafish larvae were conducted in accordance with the Animals Scientific Procedures Act 1986 (ASPA), the Animal Welfare Act 2006. All experiments were ethically approved by the University of Bristol Animal Welfare and Ethical Review Body (AWERB). Adult Zebrafish (Danio rerio) husbandry was performed as described previously[70]. Wild type and transgenic lines including Tg(mpeg:Gal4FF); Tg(UAS:NfsB-mCherry)[71,72], Tg(mpeg1:mCherryCAAX)sh378[73], Tg(*mfap4:tdTomato)* [74]were maintained on Tüpfel long fin (TL), Ekkwill (EKK), Wild-type or casper backgrounds. The mutant strain *rnaset2*^{sh532} (a kind gift from Noémie Hamilton) [40]was maintained on a nacre wild-type background or used in combination with transgenic lines as indicated. Pigmentation in larvae was avoided by 1-phenyl 2-thiourea (PTU) treatment (0.003%) from 24 hpf onwards, and replaced daily.

Wounding

Arabidopsis plants were wounded using either a 1 mm punch biopsy needle or by scratch wounding 4 times with a scalpel. Leaves were excised at the petiole with scissors and immediately placed in a 1.5 ml Eppendorf tube and snap frozen in liquid nitrogen. For scanning electron microscopy and histology, leaf 2 of Arabidopsis plants were wounded at intervals in order to collect the following timepoints concurrently at 28 dpg: 1 hpw, 24 hpw, 96 hpw, 7 days post wounding. Leaves were excised at the petiole and then placed in a 1.5 ml Eppendorf tube and covered with fixative.

For Zebrafish, needle-stick wounds were made to the dorsal somites opposite the cloaca using either a 30-gauge needle or a Micro-Tec T5 straight ultra-fine tungsten needle (Micro to Nano, Haarlem, Netherlands). To increase the signal to noise ratio for protein and RNA extraction two subsequent wounds were distributed towards the tail. Fish were then immediately placed in fresh Danieu's solution (58mM NaCl, 0.7mM KCl, 0.4mM MgSO4 0.6mM Ca(NO3)2, 5.0mM HEPES, titrated to pH7.6) for recovery.

Scanning electron microscopy

Plant samples were fixed for 15 minutes 100% methanol, and dehydrated by 2x30 minute washes in 100% dry ethanol. Zebrafish samples were fixed in 0.25% glutaraldehyde/0.025M sodium cacodylate on a rotor at 4˚ C overnight, followed by 3x5 minute washes in 0.1M sodium cacodylate buffer on a rotor before post-fixation 1% osmium/0.1 M sodium cacodylate on a rotor for 1 hour. Fixed samples were washed 2x 5 minutes 0.1 M sodium cacodylate buffer and 2x 5min ddH2O before ethanol dehydration series in 5 minute intervals (30%, 50%, 70%, 90%, 100%) and an additional 2x 10-minute washes in 100% dry ethanol. Samples underwent critical point drying then mounted on SEM stubs and coated with gold using a sputter coater. Coated samples were then imaged using a Quanta 200 (Thermo Fisher Scientific, Waltham, USA) scanning electron microscope.

Protein extraction

For Arabidopsis, three individual plants were used per condition and harvested at 21 days post germination (dpg). Arabidopsis leaves were excised from the plant and weighed. They were then added to a chilled pestle and mortar along with 1 mL of RIPA extraction buffer (50 mM Tris pH8.0, 1150 mM NaCl, undiluted 0.5% DOC, 1% NP-40, 0.1% SDS, 10x protease inhibitor, 20mg/ml PMSF) per 200 mg of wet leaf biomass. Samples were homogenised by pestle and mortar. The mixture was collected in a 1.5 ml Eppendorf tube and centrifuged at 13,000 rpm for 10 minutes at 4°C to pellet solid material. The supernatant was then collected in a clean 1.5 ml Eppendorf tube. Samples were snap frozen in liquid nitrogen and stored at -80°C.

For zebrafish, 60 larvae were used per condition and harvested at 6 days post fertilization (dpf). Tails were dissected by cutting with No.15 Disposable scalpel (Swann-Morton, Sheffield, United Kingdom) at a position just posterior to the yolk sac of the larvae. These tails were collected in 1.5 ml Eppendorf tubes. 100 µL of RIPA extraction buffer was added to the Eppendorf tube and the samples were homogenized using a Bio-Gen PRO200 tissue homogenizer (PRO scientific, Oxford, USA). Samples were snap frozen in liquid nitrogen and stored at -80°C.

Proteomics Analysis

Each sample was collected in triplicate and 100 µL of 1–2 mg/mL of protein per replicate was given to the proteomics facility for analysis. The samples were digested with trypsin and the resulting peptides labelled with Tandem Mass Tag (TMT) eleven plex reagents. The labelled samples were pooled, fractionated by high pH RP chromatography and the resulting fractions were analysed by nano-LC MSMS using an SPS-MS3 approach on an Orbitrap Fusion Lumos Mass Spectrometer (Thermo Fisher Scientific, Waltham, USA). The raw data was then analysed using the Proteome Discoverer software V2.1 (Thermo Fisher Scientific, Waltham, USA) and searched against the UniProt "*Arabidopsis thaliana*" or "*Danio rerio*" databases as well as a common contaminants database.

Candidate Search Strategy

Proteins with a significant $|Log_2FC|>1$ from our plant and animal datasets were selected for homology searches. These two subsets formed the inputs for protein BLAST searches across species against the Zebrafish or Arabidopsis proteome[75,76]. Identified proteins with significant identity were mapped back to the proteomics datasets and those proteins with a conserved change in abundance following wounding were selected for further investigation.

qRT-PCR

Zebrafish larvae, wounded or unwounded, were fixed in RNAlater™ Stabilization Solution (Thermo Fisher Scientific, Waltham, USA) prior to RNA extraction. To improve the signal to noise ratio, tails of fixed zebrafish larvae were then excised with a scalpel blade, cutting posterior to the yolk sac of the larvae. Tails were pooled in 1.5 ml Eppendorf tubes and TRIzol reagent was added before sample homogenization. Arabidopsis samples were homogenized using a microcentrifuge tube pestle in TRIzol reagent. Collected tissue was processed according to the manufacturers' protocol for 'Monarch® RNA Cleanup Kit' to isolate RNA. Yield and purity were determined using a nanodrop spectrophotometer.

cDNA synthesis was performed with Maxima First Strand cDNA Synthesis Kit for RT-qPCR with dsDNase (Thermo Fisher Scientific, Waltham, USA) or SuperScript™ IV VILO™ Master Mix with ezDNase™ Enzyme

(Thermo Fisher Scientific, Waltham, USA) according to the manufacturer's protocol.

Duplex analysis was performed using Taqman Fast advanced master mix (Thermo Fisher Scientific, Waltham, USA) and Taqman Gene expression Assays (rnaset2 - Dr03424754_m1, and eef1a1l1 - Dr03432748_m1). All assays were performed using a QuantStudio™ 3 Real-Time PCR System (Thermo Fisher Scientific, Waltham, USA).

Transmission electron microscopy

Samples were fixed in a primary fixative solution at 4˚ C overnight (4% glutaraldehyde, 1% paraformaldehyde, 0.05M sodium cacodylate, 1mM MgSO4, 1% sucrose). Fixed samples were washed in 0.1M sodium cacodylate (pH 7.4, 3x10mins) and then post fixed in 2% osmium tetroxide in 0.1M cacodylate buffer for 2 hours at room temperature. After fixation, samples were washed again in 0.1M sodium cacodylate (3x10mins). Larval zebrafish were placed on a glass slides and excess liquid removed using filter paper. A BSA/ glutaraldehyde solution was made up to a final concentration 6.75% BSA and 2.5% glutaraldehyde in 0.1M cacodylate buffer, and added to cover the larvae on the slide, and left to set for 10 minutes. Gel encased larvae were placed in water before transfer to an automatic tissue processor (Leica EM TM). The samples were processed in the automatic tissue processor, then transferred into fresh EPON, for 2–3 hours before embedding in coffin moulds and polymerised at 60°C for 24–48 hours. Blocks were then cut into sections on an Ultramicrotome (Leica EM UC6) and imaged using Talos L120C 120 kV TEM with a Ceta 16M camera (Thermo Fisher Scientific, Waltham, USA).

Histology

Leaves were submerged in botanical fix for 24 hours then washed in an ethanol series (20%, 30%, 50% and 70%) before embedding in paraffin wax. Leaves were cut in transverse sections and stained with safranin O and light green counterstain. Slides were imaged using a VS200 slide scanner (Evident, Tokyo, Japan).

Whole mount in-situ hybridization

Probes for in-situ hybridisation were designed and produced according to the PCR-based method described by Hua et al.[77]. The primer sequences are shown in Table 1 below. Whole mount in-situ hybridization was performed according to the method described by Thisse and Thisse with the following modifications[78]: Dextran sulfate was added to prehybridization and hybridization solutions to a final concentration of 5% (weight/volume); for 6 dpf larvae the wound region was excised with a scalpel blade following rehydration, 3 somites anterior and posterior of the cloaca.

Table 1
Oligonucleotides used in this work

Description	Assay	Sequence (5’-3’)
Rnaset2-Forward	ISH	AGAAGCTATTAACAGCGATCGAGA
Rnaset2-Reverse	ISH	ATTTGAACCTGGCCTCCCTG
Rnaset2-Forward + T7	ISH	CAGTGAATTGTAATACGACTCACTATAGGGAGAAGAAGCTATTAACAGCGATCGAGA
Rnaset2-Reverse + T7	ISH	CAGTGAATTGTAATACGACTCACTATAGGGAGAATTTGAACCTGGCCTCCCTG

Fluorescence in situ hybridization combined with immunofluorescence

Fluorescent in situ hybridization was performed as described in[79]. Antibodies used for immunofluorescence were as follows: 1:250, Anti-RFP pAb, purified lgG/Rabbit (RFP) (PM005, MBL) and 1:500, Alexa Fluor 488 goat anti rabbit (A11034, Invitrogen).

TUNEL assay

TUNEL assay was performed using the ApopTag® Red In Situ Apoptosis Detection Kit (S7165, Merck, Darmstadt, Germany). Samples were protected from light where possible throughout processing. Zebrafish Larvae fixed in 4% (weight/volume) PFA for 1 hour at room temperature PBSTX (1x PBS, 0.5% v/v Triton X-100) (3x5 min). PBSTX were permeabilized with prechilled 2:1 Ethanol:Acetic acid solution and samples were incubated at -20 ˚ C for 15 minutes. Samples were then washed PBSTX (3x5 min). PBSTX was replaced with Equilibration buffer and samples were incubated for 1 hour at room temperature with gentle rocking. Equilibration buffer was then replaced with 110 µL TdT enzyme mix (30% TdT enzyme, 70% Reaction buffer) and samples were incubated at 37˚ C overnight. The enzyme mix was then removed, and samples were washed briefly in PBSTX. PBSTX was then removed and replaced with 100 µL stop/wash buffer and samples were incubated for 5 minutes. Samples were then washed in PBSTX for (10x5 min). Samples were blocked in 34 µL of block solution for 2h at room temperature and agitating occasionally by gently flicking the tubes. Blocking solution was replaced with 65 µL Anti-Dig solution (31 µL anti-digoxigenin rhodamine, 34 µL Blocking solution) and samples were incubated overnight at 4˚ C. Samples were washed PBSTX (4x5 min), then incubated in 400 µL block solution (10% Goat serum in PBSTX) for 2–3 hours at room temperature. Block solution was replaced with primary antibody (1:250, Anti-RFP pAb, purified lgG/Rabbit (RFP) (PM005, MBL)) and samples were incubated overnight at 4˚ C. Samples were washed briefly in PBSTX (3x), then for a further (6x30 min). Samples were blocked in 300 µL of block solution for 1 hour at room temperature. Block solution was replaced with 400 µL of secondary antibody (1:500, Alexa Fluor 488 goat anti rabbit, A11034, Invitrogen) and incubated overnight at 4˚ C with gentle rocking. Samples were briefly in PBSTX (3x), then for a further (6x30 min). Samples were stored in PBSTX for up to five days before imaging.

Confocal Microscopy

Images were captured with a Leica SP8 AOBS confocal laser scanning microscope attached to a Leica DM I6000 inverted epifluorescence microscope using a 40x HC PL APO CS2 lens in oil. For live samples, zebrafish larvae (3–6 dpf) were mounted laterally in 1% low-gelling temperature agarose (Sigma Aldrich, Burlington, USA) in a glass bottomed dish which was filled with 0.1 mg/mL MS-222 in Danieu's solution. For fixed samples, whole or dissected tissue from Zebrafish larvae (3–6 dpf) was mounted laterally in 1% low gelling temperature agarose in a glass bottomed dish and covered with a few drops of 1X PBS to prevent the agarose dehydrating.

Lysotracker

To selectively stain the lysosomes of 6 dpf zebrafish larvae, LysoTracker™ Green DND-26 (Invitrogen, Waltham, USA) was diluted 1:100 in Danieu's solution. Larvae were incubated in this staining solution at 28˚ C for 45 minutes then washed in fresh Danieu's solution for (3x3 min).

Post-Image Analysis

Image analysis was performed in Fiji[80]. The Modular image analysis (MIA) plugin [81] was used to create custom workflows for segmentation, 2D and 3D measurements. Statistics All values are presented as mean values, and error bars represent standard error of the mean (SEM) or 95% confidence intervals unless otherwise indicated. P values were calculated using unpaired two-tailed Mann-Whitney unless otherwise indicated. All experiments were independently repeated.

Whole-plant ROS imaging

Whole-plant live imaging of reactive oxygen species (ROS) was monitored using the fluorogenic cell-permeable probe H2DCFDA (2′,7′-dichlorodihydrofluorescein diacetate), as described previously[82], with the following modifications. Plants were fumigated in a sealed plastic container (71 × 44 × 38 cm) with 50 µM H2DCFDA (Millipore-Sigma, St. Louis, MO, USA) in 50 mM phosphate buffer (pH 7.4) using a portable mini nebulizer (YS35, VapoZen) for 30 min. Following fumigation, leaves of 3-4-week-old plants were wounded using a sterile 10 µl pipette tip by piercing through the leaf. Images were taken prior to wounding and then time-lapse images were recorded every 5 seconds using a DP74 camera (Olympus, Tokyo, Japan) mounted on a MZFLIII fluorescence microscope (Leica, Wetzlar, Germany) with a GFP filter (excitation/emission 495 nm/517 nm). All images within an experiment were acquired using identical acquisition settings.

Electrolyte leakage assays

Electrolyte leakage experiments were performed as described in [83] with the following modifications. Briefly, 9 mm leaf discs were collected using a cork borer and placed abaxial side up in sterile water. For wound-associated assays, the collection of measurements began immediately without equilibration. For infection-associated assays, leaf discs were equilibrated in water for 1 hour then vacuum infiltrated with water or *Xcc*Race6 suspension (10^8 CFU mL^{-1}) in a 5 ml syringe. Following infiltration, leaf discs were transferred to a fresh petri dish containing sterile water before readings began. Measurements were recorded using a LAQUAtwin-EC-11 compact conductivity meter (Horiba, Kyoto, Japan).

Wound Infection and fluorescence microscopy

Wound inoculation assay was performed as previously reported [84] with the following modifications. Leaves of 3-4-week-old Arabidopsis plants were wounded using a sterile 10 µl pipette tip by piercing through the leaf. Wound sites were immediately inoculated with 1 µl of GFP-expressing *Xcc*Race6 suspension (10^9 CFU mL^{-1}). Plants were incubated at 22°C without covering, and GFP fluorescence was detected at the indicated time points using a MZFLIII fluorescence microscope (Leica, Wetzlar, Germany) equipped with a GFP filter. All experiments were performed using identical acquisition settings using the imaging software cellSense (Evident, Tokyo, Japan).

AlphaFold model protein structure comparison in ChimeraX

Prediction models of the structure of zebrafish Rnaset2 (B8XY56) and Arabidopsis RNS1 (P42813) proteins were retrieved from AlphaFold[85]. The AphaFold prediction models AF-B8XY56-F1-v6 (pLDDT = 88.25) for zebrafish Rnaset2, and AF-P42813-F1-v6 (pLDDT = 93) for Arabidopsis RNS1 were compared in UCSF ChimeraX, using the matchmaker function, and both models were pseudocoloured by RMSD[86].

Declarations

Data availability

The mass spectrometry proteomics data for this study have been deposited to the ProteomeXchange Consortium via the PRIDE [87] partner repository with the dataset identifier PXD080984.

Acknowledgements

We thank N. Hamilton for sharing the *rnaset2*^{sh532}zebrafish line. We thank M. Grant for providing *Xcc*Race6. The authors also thank members of the Wolfson Bioimaging Facility (University of Bristol, UK) for their help with imaging and image analysis, the Histology services unit (University of Bristol, UK) and the Zebrafish Facility of the University of Bristol for their services and contribution. Funding: This work was supported by the Scar Free Foundation (to T.B., O.A.P and P.M.), the Wellcome Trust (to T.B. and P.M.), the Bristol Center for Agricultural Innovation (to P.B.), and The Royal Society (to P.B.). Author contributions: P.B., and P.M., conceived of the project; T.B., O.A.P., A.P., and P.B. performed experiments; P.L. and K.H. performed proteomic analysis; A.P. and K.F. provided materials; and T.B., P.B. and P.M. wrote the manuscript with input from all authors.

Competing interests

P.M. is a member of the editorial board for *npj Regenerative Medicine*. The authors declare no other competing interests.

Author Contribution

P.B., and P.M., conceived of the project; T.B., O.A.P., A.P., and P.B. performed experiments; P.L. and K.H. performed proteomic analysis; A.P. and K.F. provided materials; and T.B., P.B. and P.M. wrote the manuscript with input from all authors.

References

1. Rodrigues, M., Kosaric, N., Bonham, C. & Gurtner, G. WOUND HEALING: A CELLULAR PERSPECTIVE. *PHYSIOLOGICAL REVIEWS* 99, 665–706 (2019). https://doi.org/10.1152/physrev.00067.2017
2. George, A. & Martin, P. Wound Healing Insights from Flies and Fish. *Cold Spring Harbor Perspectives in Biology* 14 (2022). https://doi.org/10.1101/cshperspect.a041217
3. Peña, O. A. & Martin, P. Cellular and molecular mechanisms of skin wound healing. *Nature Reviews Molecular Cell Biology* (2024). https://doi.org/10.1038/s41580-024-00715-1
4. Nunan, R. *et al.* Ephrin-Bs Drive Junctional Downregulation and Actin Stress Fiber Disassembly to Enable Wound Re-epithelialization. *Cell Reports* 13, 1380–1395 (2015). https://doi.org/10.1016/j.celrep.2015.09.085
5. Park, S. *et al.* Tissue-scale coordination of cellular behaviour promotes epidermal wound repair in live mice. *Nature Cell Biology* 19, 155–163 (2017). https://doi.org/10.1038/ncb3472
6. Niethammer, P., Grabher, C., Look, A. T. & Mitchison, T. J. A tissue-scale gradient of hydrogen peroxide mediates rapid wound detection in zebrafish. *Nature* 459, 996-U123 (2009). https://doi.org/10.1038/nature08119
7. Moreira, S., Stramer, B., Evans, I., Wood, W. & Martin, P. Prioritization of Competing Damage and Developmental Signals by Migrating Macrophages in the Drosophila Embryo. *Current Biology* 20, 464–470 (2010). https://doi.org/10.1016/j.cub.2010.01.047
8. Wong, V., Akaishi, S., Longaker, M. & Gurtner, G. Pushing Back: Wound Mechanotransduction in Repair and Regeneration. *JOURNAL OF INVESTIGATIVE DERMATOLOGY* 131, 2186–2196 (2011). https://doi.org/10.1038/jid.2011.212
9. Ferguson, M. W. J. & O'Kane, S. Scar-free healing: from embryonic mechanisms to adult therapeutic intervention. *Philosophical Transactions of the Royal Society B-Biological Sciences* 359, 839–850 (2004). https://doi.org/10.1098/rstb.2004.1475
10. Martin, P. *et al.* Wound healing in the PU.1 null mouse - Tissue repair is not dependent on inflammatory cells. *Current Biology* 13, 1122–1128 (2003). https://doi.org/10.1016/s0960-9822(03)00396-8
11. Bevan, L. *et al.* Specific macrophage populations promote both cardiac scar deposition and subsequent resolution in adult zebrafish. *Cardiovasc Res* 116, 1357–1371 (2020). https://doi.org/10.1093/cvr/cvz221
12. Aurora, A. B. *et al.* Macrophages are required for neonatal heart regeneration. *J Clin Invest* 124, 1382–1392 (2014). https://doi.org/10.1172/JCI72181
13. Eming, S. A., Krieg, T. & Davidson, J. M. Inflammation in wound repair: Molecular and cellular mechanisms. *Journal of Investigative Dermatology* 127, 514–525 (2007). https://doi.org/10.1038/sj.jid.5700701
14. Martin, P. & Nunan, R. Cellular and molecular mechanisms of repair in acute and chronic wound healing. *British Journal of Dermatology* 173, 370–378 (2015). https://doi.org/10.1111/bjd.13954
15. Lämmermann, T. In the eye of the neutrophil swarm-navigation signals that bring neutrophils together in inflamed and infected tissues. *JOURNAL OF LEUKOCYTE BIOLOGY* 100, 55–63 (2016). https://doi.org/10.1189/jlb.1MR0915-403

16. Aragona, M. *et al.* Defining stem cell dynamics and migration during wound healing in mouse skin epidermis. *Nat Commun* 8, 14684 (2017). https://doi.org/10.1038/ncomms14684
17. Rognoni, E. *et al.* Fibroblast state switching orchestrates dermal maturation and wound healing. *Molecular Systems Biology* 14 (2018). https://doi.org/10.15252/msb.20178174
18. Weavers, H. & Martin, P. The cell biology of inflammation: From common traits to remarkable immunological adaptations. *Journal of Cell Biology* 219 (2020). https://doi.org/10.1083/jcb.202004003
19. Ikeuchi, M. *et al.* Wound-inducible WUSCHEL-RELATED HOMEOBOX 13 is required for callus growth and organ reconnection. *Plant Physiology* 188, 425–441 (2022). https://doi.org/10.1093/plphys/kiab510
20. Zhang, A. *et al.* Cell-wall damage activates DOF transcription factors to promote wound healing and tissue regeneration in < i>Arabidopsis thaliana. *Current Biology* 32, 1883-+ (2022). https://doi.org/10.1016/j.cub.2022.02.069
21. Maekawa, T., Kashkar, H. & Coll, N. Dying in self-defence: a comparative overview of immunogenic cell death signalling in animals and plants. *CELL DEATH AND DIFFERENTIATION* 30, 258–268 (2023). https://doi.org/10.1038/s41418-022-01060-6
22. Koenig, M., Laia, H., Doehlemann, G. & Villamil, J. Processing and release of endogenous immunogenic peptide signals. *PLANT JOURNAL* 126 (2026). https://doi.org/10.1111/tpj.70897
23. Byatt, T. C. & Martin, P. Parallel repair mechanisms in plants and animals. *Disease Models & Mechanisms* 16 (2023). https://doi.org/10.1242/dmm.049801
24. Razzell, W., Evans, Iwan R., Martin, P. & Wood, W. Calcium Flashes Orchestrate the Wound Inflammatory Response through DUOX Activation and Hydrogen Peroxide Release. *Current Biology* 23, 424–429 (2013). https://doi.org/10.1016/j.cub.2013.01.058
25. Suda, H. & Toyota, M. Integration of long-range signals in plants: A model for wound-induced Ca < SUP>2+ </SUP>, electrical, ROS, and glutamate waves. *Current Opinion in Plant Biology* 69 (2022). https://doi.org/10.1016/j.pbi.2022.102270
26. Kramer, A., Green, J., Pollard, J. & Tugendreich, S. Causal analysis approaches in Ingenuity Pathway Analysis. *Bioinformatics* 30, 523–530 (2014). https://doi.org/10.1093/bioinformatics/btt703
27. Hanahan, D. & Weinberg, R. A. Hallmarks of Cancer: The Next Generation. *Cell* 144, 646–674 (2011). https://doi.org/10.1016/j.cell.2011.02.013
28. MacCarthy-Morrogh, L. & Martin, P. The hallmarks of cancer are also the hallmarks of wound healing. *Science Signaling* 13 (2020). https://doi.org/10.1126/scisignal.aay8690
29. Wu, T. Z. *et al.* clusterProfiler 4.0: A universal enrichment tool for interpreting omics data. *Innovation* 2 (2021). https://doi.org/10.1016/j.xinn.2021.100141
30. Yu, G. C., Wang, L. G., Han, Y. Y. & He, Q. Y. clusterProfiler: an R Package for Comparing Biological Themes Among Gene Clusters. *Omics-a Journal of Integrative Biology* 16, 284–287 (2012). https://doi.org/10.1089/omi.2011.0118
31. Bennett, F., Stroud, E., Kachroo, P. & Grant, M. Systemic acquired resistance: an emerging role for jasmonates in local signal biogenesis, translocation and distal signal decoding. *NEW PHYTOLOGIST* 251, 3142–3158 (2026). https://doi.org/10.1111/nph.71405

32. Sweat, T. A. & Wolpert, T. J. Thioredoxin < i > h</i > 5 is required for victorin sensitivity mediated by a CC-NBS-LRR gene in < i>Arabidopsis. *Plant Cell* 19, 673–687 (2007). https://doi.org/10.1105/tpc.106.047563
33. Saad, I. *et al.* Thioredoxin-1 augments wound healing and promote angiogenesis in a murine ischemic full-thickness wound model. *Surgery* 164, 1077–1086 (2018). https://doi.org/10.1016/j.surg.2018.05.045
34. Korte, B. G. *et al.* Cell Type-Specific Transcriptome Profiling Reveals a Role for Thioredoxin During Tumor Initiation. *Frontiers in Immunology* 13 (2022). https://doi.org/10.3389/fimmu.2022.818893
35. Hillwig, M. S., LeBrasseur, N. D., Green, P. J. & MacIntosh, G. C. Impact of transcriptional, ABA-dependent, and ABA-independent pathways on wounding regulation of RNS1 expression. *Molecular Genetics and Genomics* 280, 249–261 (2008). https://doi.org/10.1007/s00438-008-0360-3
36. Goodman, H. L. *et al.* Extracellular ATP targets Arabidopsis RIBONUCLEASE 1 to suppress mycotoxin stress-induced cell death. *New Phytologist* 235, 1531–1542 (2022). https://doi.org/10.1111/nph.18211
37. Liu, P. P. *et al.* Mammalian mitochondrial RNAs are degraded in the mitochondrial intermembrane space by RNASET2. *Protein & Cell* 8, 735–749 (2017). https://doi.org/10.1007/s13238-017-0448-9
38. Greulich, W. *et al.* TLR8 Is a Sensor of RNase T2 Degradation Products. *CELL* 179, 1264-+ (2019). https://doi.org/10.1016/j.cell.2019.11.001
39. Rutherford, H., Candeias, D., Duncan, C., Renshaw, S. & Hamilton, N. Macrophage transplantation rescues RNASET2-deficient leukodystrophy by replacing deficient microglia in a zebrafish model. *PROCEEDINGS OF THE NATIONAL ACADEMY OF SCIENCES OF THE UNITED STATES OF AMERICA* 121 (2024). https://doi.org/10.1073/pnas.2321496121
40. Hamilton, N. *et al.* The failure of microglia to digest developmental apoptotic cells contributes to the pathology of RNASET2-deficient leukoencephalopathy. *Glia* 68, 1531–1545 (2020). https://doi.org/10.1002/glia.23829
41. Weiss-Gayet, M. *et al.* Restorative macrophage-derived RNAseT2 stimulates muscle stem cell fusion via an SLK/N-WASP/actin bundling dependent axis. *NATURE COMMUNICATIONS* 17 (2026). https://doi.org/10.1038/s41467-026-71990-z
42. Sur, A. *et al.* Single-cell analysis of shared signatures and transcriptional diversity during zebrafish development. *DEVELOPMENTAL CELL* 58 (2023). https://doi.org/10.1016/j.devcel.2023.11.001
43. Megel, C. *et al.* Plant RNases T2, but not Dicer-like proteins, are major players of tRNA-derived fragments biogenesis. *NUCLEIC ACIDS RESEARCH* 47, 941–952 (2019). https://doi.org/10.1093/nar/gky1156
44. Hillwig, M. *et al.* RNS2, a conserved member of the RNase T2 family, is necessary for ribosomal RNA decay in plants. *PROCEEDINGS OF THE NATIONAL ACADEMY OF SCIENCES OF THE UNITED STATES OF AMERICA* 108, 1093–1098 (2011). https://doi.org/10.1073/pnas.1009809108
45. Bariola, P., MacIntosh, G. & Green, P. Regulation of S-like ribonuclease levels in arabidopsis. Antisense inhibition of RNS1 or RNS2 elevates anthocyanin accumulation. *PLANT PHYSIOLOGY* 119, 331–342 (1999). https://doi.org/10.1104/pp.119.1.331
46. Fichman, Y. & Mittler, R. Integration of electric, calcium, reactive oxygen species and hydraulic signals during rapid systemic signaling in plants. *Plant Journal* 107, 7–20 (2021). https://doi.org/10.1111/tpj.15360
47. Buscaill, P. *et al.* Subtilase SBT5.2 inactivates flagellin immunogenicity in the plant apoplast. *NATURE COMMUNICATIONS* 15 (2024). https://doi.org/10.1038/s41467-024-54790-1

48. Baranzini, N. *et al.* Antimicrobial Role of RNASET2 Protein During Innate Immune Response in the Medicinal Leech Hirudo verbana. *Front Immunol* 11, 370 (2020). https://doi.org/10.3389/fimmu.2020.00370
49. Miyake, K., Shibata, T., Ohto, U. & Shimizu, T. Emerging roles of the processing of nucleic acids and Toll-like receptors in innate immune responses to nucleic acids. *JOURNAL OF LEUKOCYTE BIOLOGY* 101, 135–142 (2017). https://doi.org/10.1189/jlb.4MR0316-108R
50. Roers, A., Hiller, B. & Hornung, V. Recognition of Endogenous Nucleic Acids by the Innate Immune System. *IMMUNITY* 44, 739–754 (2016). https://doi.org/10.1016/j.immuni.2016.04.002
51. Bérouti, M. *et al.* Lysosomal endonuclease RNase T2 and PLD exonucleases cooperatively generate RNA ligands for TLR7 activation. *IMMUNITY* 57 (2024). https://doi.org/10.1016/j.immuni.2024.04.010
52. Ostendorf, T. *et al.* Immune Sensing of Synthetic, Bacterial, and Protozoan RNA by Toll-like Receptor 8 Requires Coordinated Processing by RNase T2 and RNase 2. *IMMUNITY* 52, 591-+ (2020). https://doi.org/10.1016/j.immuni.2020.03.009
53. Gomez-Diaz, C. *et al.* RNase T2 restricts TLR13-mediated autoinflammation in vivo. *JOURNAL OF EXPERIMENTAL MEDICINE* 222 (2025). https://doi.org/10.1084/jem.20241424
54. Ortega-Gómez, A., Perretti, M. & Soehnlein, O. Resolution of inflammation: an integrated view. *Embo Molecular Medicine* 5, 661–674 (2013). https://doi.org/10.1002/emmm.201202382
55. Headland, S. E. & Norling, L. V. The resolution of inflammation: Principles and challenges. *Seminars in Immunology* 27, 149–160 (2015). https://doi.org/10.1016/j.smim.2015.03.014
56. Gurevich, D. B. *et al.* Live imaging of wound angiogenesis reveals macrophage orchestrated vessel sprouting and regression. *Embo Journal* 37 (2018). https://doi.org/10.15252/embj.201797786
57. Wang, P. *et al.* Evolution of GOLDEN2-LIKE gene function in C3 and C4 plants. *PLANTA* 237, 481–495 (2013). https://doi.org/10.1007/s00425-012-1754-3
58. Paps, J., Xu, F., Zhang, G. & Holland, P. Reinforcing the Egg-Timer: Recruitment of Novel Lophotrochozoa Homeobox Genes to Early and Late Development in the Pacific Oyster. *GENOME BIOLOGY AND EVOLUTION* 7, 677–688 (2015). https://doi.org/10.1093/gbe/evv018
59. Greiff, G., Bethell, M., Clark, J. & Harrison, C. Report WOX neofunctionalization following an ancient duplication in mosses. *CURRENT BIOLOGY* 36, 3388–3397 (2026). https://doi.org/10.1016/j.cub.2026.05.045
60. Holland, P., Marlétaz, F., Maeso, I., Dunwell, T. & Paps, J. New genes from old: asymmetric divergence of gene duplicates and the evolution of development. *PHILOSOPHICAL TRANSACTIONS OF THE ROYAL SOCIETY B-BIOLOGICAL SCIENCES* 372 (2017). https://doi.org/10.1098/rstb.2015.0480
61. Olvera-Carrillo, Y. *et al.* A Conserved Core of Programmed Cell Death Indicator Genes Discriminates Developmentally and Environmentally Induced Programmed Cell Death in Plants. *PLANT PHYSIOLOGY* 169, 2684–2699 (2015). https://doi.org/10.1104/pp.15.00769
62. LeBrasseur, N. D., MacIntosh, G. C., Perez-Amador, M. A., Saitoh, M. & Green, P. J. Local and systemic wound-induction of RNase and nuclease activities in Arabidopsis: RNS1 as a marker for a JA-independent systemic signaling pathway. *Plant Journal* 29, 393–403 (2002). https://doi.org/10.1046/j.1365-313x.2002.01223.x

63. Pareja, L., Galvez-Valdivieso, G., Piedras, P. & Diaz-Baena, M. Mechanical Wounding Induces Rapid RNA-Degrading Activity Mediated by the S-like Ribonuclease PvRNS2 in Common Bean. *PLANTS-BASEL* 15 (2026). https://doi.org/10.3390/plants15121907
64. Chai, J., Wang, Y. & Wang, Y. Mechanisms and balanced regulation of plant immunity. *NATURE REVIEWS MOLECULAR CELL BIOLOGY* (2026). https://doi.org/10.1038/s41580-026-01009-4
65. Chen, C. *et al.* Extracellular plant subtilases dampen cold-shock peptide elicitor levels. *NATURE PLANTS* 10 (2024). https://doi.org/10.1038/s41477-024-01815-8
66. Wang, C., Chen, W., Aili, M., Zhu, L. & Chen, Y. tRNA-derived small RNAs in plant response to biotic and abiotic stresses. *FRONTIERS IN PLANT SCIENCE* 14 (2023). https://doi.org/10.3389/fpls.2023.1131977
67. BARIOLA, P. *et al.* THE ARABIDOPSIS RIBONUCLEASE GENE RNS1 IS TIGHTLY CONTROLLED IN RESPONSE TO PHOSPHATE LIMITATION. *PLANT JOURNAL* 6, 673–685 (1994). https://doi.org/10.1046/j.1365-313X.1994.6050673.x
68. TAYLOR, C., BARIOLA, P., DELCARDAYRE, S., RAINES, R. & GREEN, P. RNS2 - A SENESCENCE-ASSOCIATED RNASE OF ARABIDOPSIS THAT DIVERGED FROM THE S-RNASES BEFORE SPECIATION. *PROCEEDINGS OF THE NATIONAL ACADEMY OF SCIENCES OF THE UNITED STATES OF AMERICA* 90, 5118–5122 (1993). https://doi.org/10.1073/pnas.90.11.5118
69. Huot, B., Yao, J., Montgomery, B. L. & He, S. Y. Growth-Defense Tradeoffs in Plants: A Balancing Act to Optimize Fitness. *Molecular Plant* 7, 1267–1287 (2014). https://doi.org/10.1093/mp/ssu049
70. Westerfield, M. *The Zebrafish Book. A Guide for the Laboratory Use of Zebrafish (Danio rerio)*. 5th Edition edn, (University of Oregon Press, Eugene, 2007).
71. Davison, J. M. *et al.* Transactivation from Gal4-VP16 transgenic insertions for tissue-specific cell labeling and ablation in zebrafish. *Developmental Biology* 304, 811–824 (2007). https://doi.org/10.1016/j.ydbio.2007.01.033
72. Palha, N. *et al.* Real-Time Whole-Body Visualization of Chikungunya Virus Infection and Host Interferon Response in Zebrafish. *Plos Pathogens* 9 (2013). https://doi.org/10.1371/journal.ppat.1003619
73. Bojarczuk, A. *et al.* Cryptococcus neoformans Intracellular Proliferation and Capsule Size Determines Early Macrophage Control of Infection. *Sci Rep* 6, 21489 (2016). https://doi.org/10.1038/srep21489
74. Walton, E., Cronan, M., Beerman, R. & Tobin, D. The Macrophage-Specific Promoter mfap4 Allows Live, Long-Term Analysis of Macrophage Behavior during Mycobacterial Infection in Zebrafish. *PLOS ONE* 10 (2015). https://doi.org/10.1371/journal.pone.0138949
75. Johnson, M. *et al.* NCBIBLAST: a better web interface. *Nucleic Acids Research* 36, W5-W9 (2008). https://doi.org/10.1093/nar/gkn201
76. Camacho, C. *et al.* BLAST plus: architecture and applications. *Bmc Bioinformatics* 10 (2009). https://doi.org/10.1186/1471-2105-10-421
77. Hua, R. F., Yu, S. S., Liu, M. G. & Li, H. H. A PCR-Based Method for RNA Probes and Applications in Neuroscience. *Frontiers in Neuroscience* 12 (2018). https://doi.org/10.3389/fnins.2018.00266
78. Thisse, C. & Thisse, B. High-resolution in situ hybridization to whole-mount zebrafish embryos. *Nature Protocols* 3, 59–69 (2008). https://doi.org/10.1038/nprot.2007.514

79. He, J., Mo, D., Chen, J. & Luo, L. Combined whole-mount fluorescence in situ hybridization and antibody staining in zebrafish embryos and larvae. *Nature Protocols* 15, 3361–3379 (2020). https://doi.org/10.1038/s41596-020-0376-7
80. Schindelin, J. *et al.* Fiji: an open-source platform for biological-image analysis. *Nature Methods* 9, 676–682 (2012). https://doi.org/10.1038/nmeth.2019
81. Cross, S. J., Fisher, J. & Jepson, M. A. ModularImageAnalysis (MIA): Assembly of modularised image and object analysis workflows in ImageJ. *Journal of Microscopy* (2023). https://doi.org/10.1111/jmi.13227
82. Fichman, Y., Miller, G. & Mittler, R. Whole-Plant Live Imaging of Reactive Oxygen Species. *MOLECULAR PLANT* 12, 1203–1210 (2019). https://doi.org/10.1016/j.molp.2019.06.003
83. Bach-Pages, M. & Preston, G. in *HOST-PATHOGEN INTERACTIONS: METHODS AND PROTOCOLS* Vol. 1734 *Methods in Molecular Biology* 241–255 (2018).
84. Misas-Villamil, J. *et al.* Pseudomonas syringae pv. syringae Uses Proteasome Inhibitor Syringolin A to Colonize from Wound Infection Sites. *PLOS PATHOGENS* 9 (2013). https://doi.org/10.1371/journal.ppat.1003281
85. Bertoni, D. *et al.* AlphaFold Protein Structure Database 2025: a redesigned interface and updated structural coverage. *Nucleic Acids Research* 54, D358-D362 (2026). https://doi.org/10.1093/nar/gkaf1226
86. Meng, E. C. *et al.* UCSF ChimeraX: Tools for structure building and analysis. *Protein Science* 32, e4792 (2023). https://doi.org/https://doi.org/10.1002/pro.4792
87. Perez-Riverol, Y. *et al.* The PRIDE database at 20 years: 2025 update. *NUCLEIC ACIDS RESEARCH* 53, D543-D553 (2024). https://doi.org/10.1093/nar/gkae1011

Figures

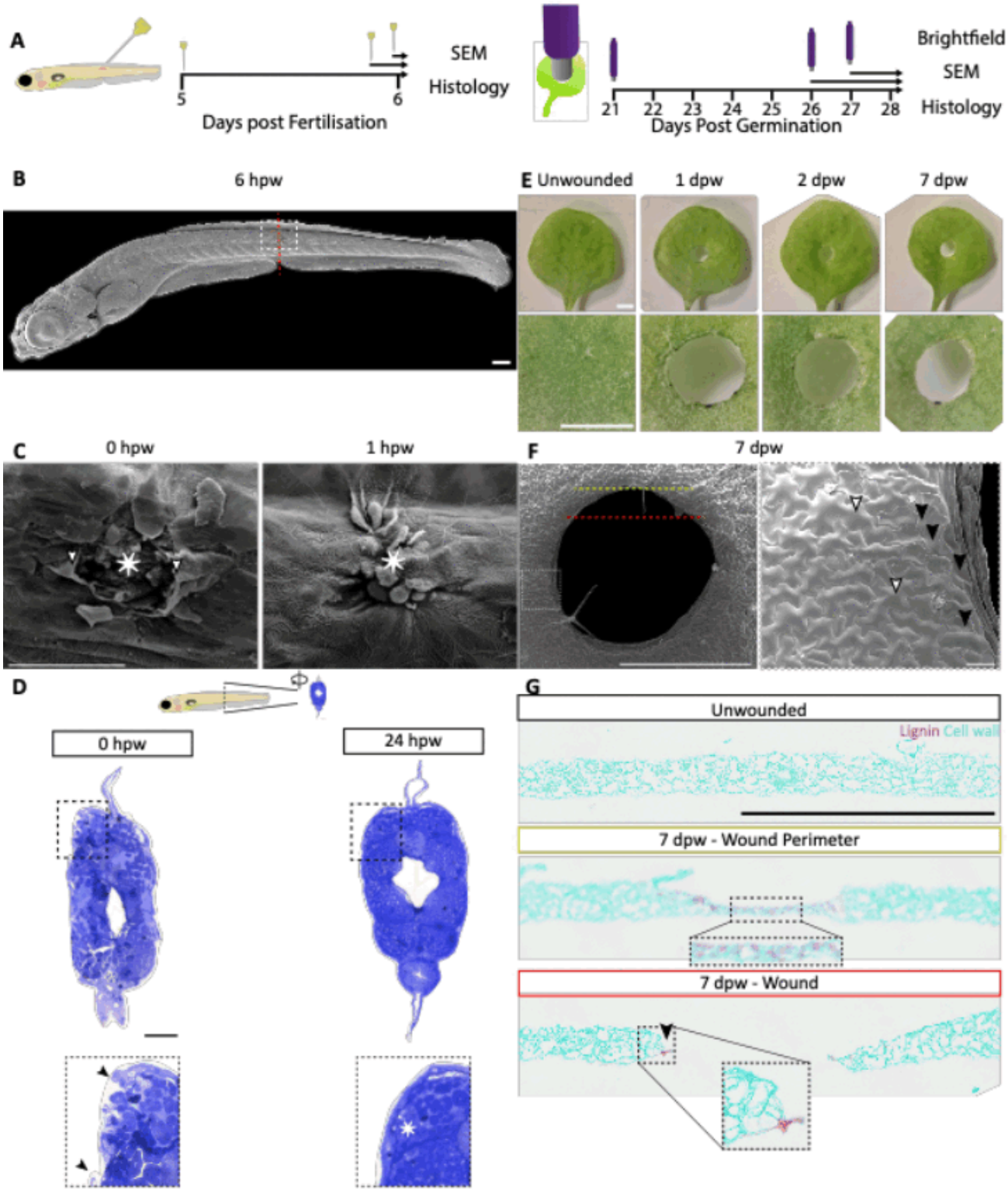


Figure 1

Arabidopsis and zebrafish exhibit distinct morphological responses to tissue wounding.

(A) Experimental workflow for wounding and tissue collection from zebrafish and Arabidopsis for Scanning electron microscopy (SEM) and histological analysis. **(B)** SEM of a 6-day-post-fertilisation (dpf) zebrafish larva at 6 hpw. The white box indicates the region shown at higher magnification in (C), and the red dashed line indicates the position of the transverse sections shown in (D). **(C)** Higher-magnification SEM images of

zebrafish wounds immediately after wounding (0 hpw) and at 1 hpw. White asterisks indicate the wound centre, and white arrowheads indicate the epithelial wound margins. **(D)** Methylene Blue stained resin sections through flank regions of wounded zebrafish larvae (6 dpf) at 0 and 24 hpw. Black arrowheads indicate epithelial wound margins, and the white asterisk indicates newly formed healing tissue. **(E)** Brightfield images of Arabidopsis leaves before wounding (unwounded) and at 1, 2 and 7 days post-wounding (dpw). **(F)** SEM of an *Arabidopsis* leaf wound at 7 dpw. The boxed region is shown at higher magnification; black arrowheads indicate deflated cells at the wound margin, and white arrowheads indicate healthy cells away from the wound. **(G)** Histological sections of unwounded and wounded Arabidopsis leaves at 7 dpw stained with Safranin O, corresponding to dashed lines in (C) at the wound perimeter (yellow line) and within the wound (red line). **Scale bars:** (B-D) = 1 mm; (C, inset) = 50 μm; (E') = 100 μm; (E'', F) = 50 μm.

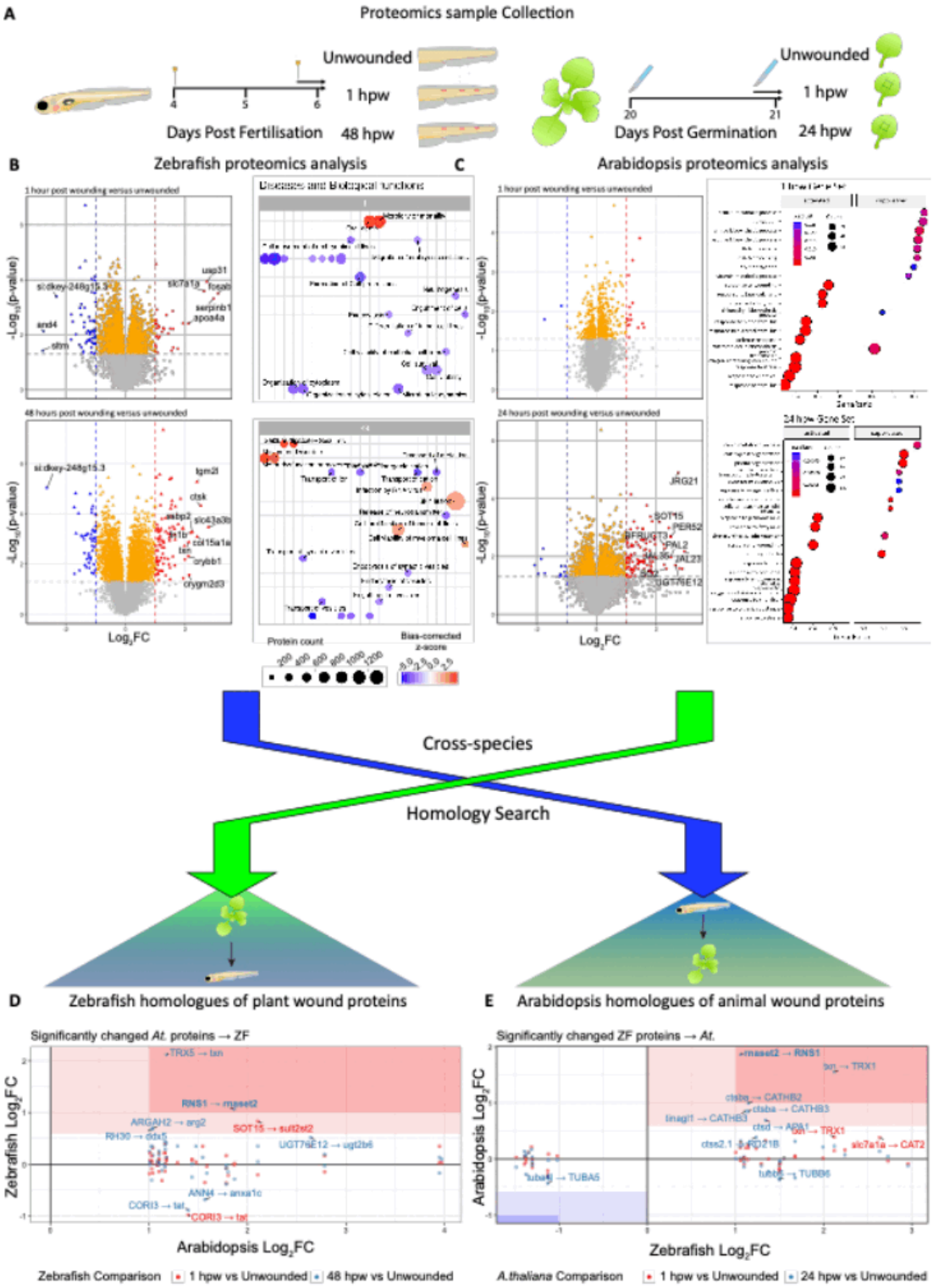


Figure 2

Reciprocal cross-kingdom proteomics identifies conserved wound-responsive proteins.

(A) Experiment design for comparative proteomic analysis of wound responses in zebrafish and Arabidopsis. Zebrafish and Arabidopsis were sampled before wounding (unwounded) and the indicated times post-wounding (hpw). Proteins were digested with trypsin and analysed by mass spectrometry. **(B)** Differential

protein abundance and pathway analysis in wounded zebrafish tissue. Log_2 fold change (log_2FC) in protein abundance versus $-log_{10}(P)$ at 1 and 48 hpw relative to unwounded controls. Vertical dashed lines indicate $log_2FC = -1$ and +1; horizontal dashed lines indicate $P = 0.05$. Diseases and Biological Functions identified by Qiagen Ingenuity Pathway Analysis, shown for annotations with bias-corrected *z*-scores ≥ |2|. **(C)** Differential protein abundance and gene set enrichment analysis in wounded Arabidopsis tissue. Log_2FC in protein abundance versus $-log_{10}(P)$ at 1 and 24 hpw relative to unwounded controls. Vertical dashed lines indicate $log_2FC = -1$ and +1. Gene ontology (GO) terms enriched among proteins showing altered abundance ($P < 0.05$) at 1 or 24 hpw. **(D)** Reciprocal orthologue analysis of Arabidopsis wound-responsive proteins. Log_2FC in Arabidopsis (x-axis) is plotted against log_2FC of their zebrafish homologues (y-axis). Highlighted regions indicate conserved increases in protein abundance ($log_2FC \geq 0.6$ and ≥1). **(E)** Reciprocal orthologue analysis of zebrafish wound-responsive proteins. Log_2FC in zebrafish (x-axis) is plotted against log_2FC of their Arabidopsis homologues (y-axis). Highlighted regions indicate $log_2FC \geq 0.6$ or ≥1 (increased abundance) and ≤ −0.6 or ≤ −1 (decreased abundance).

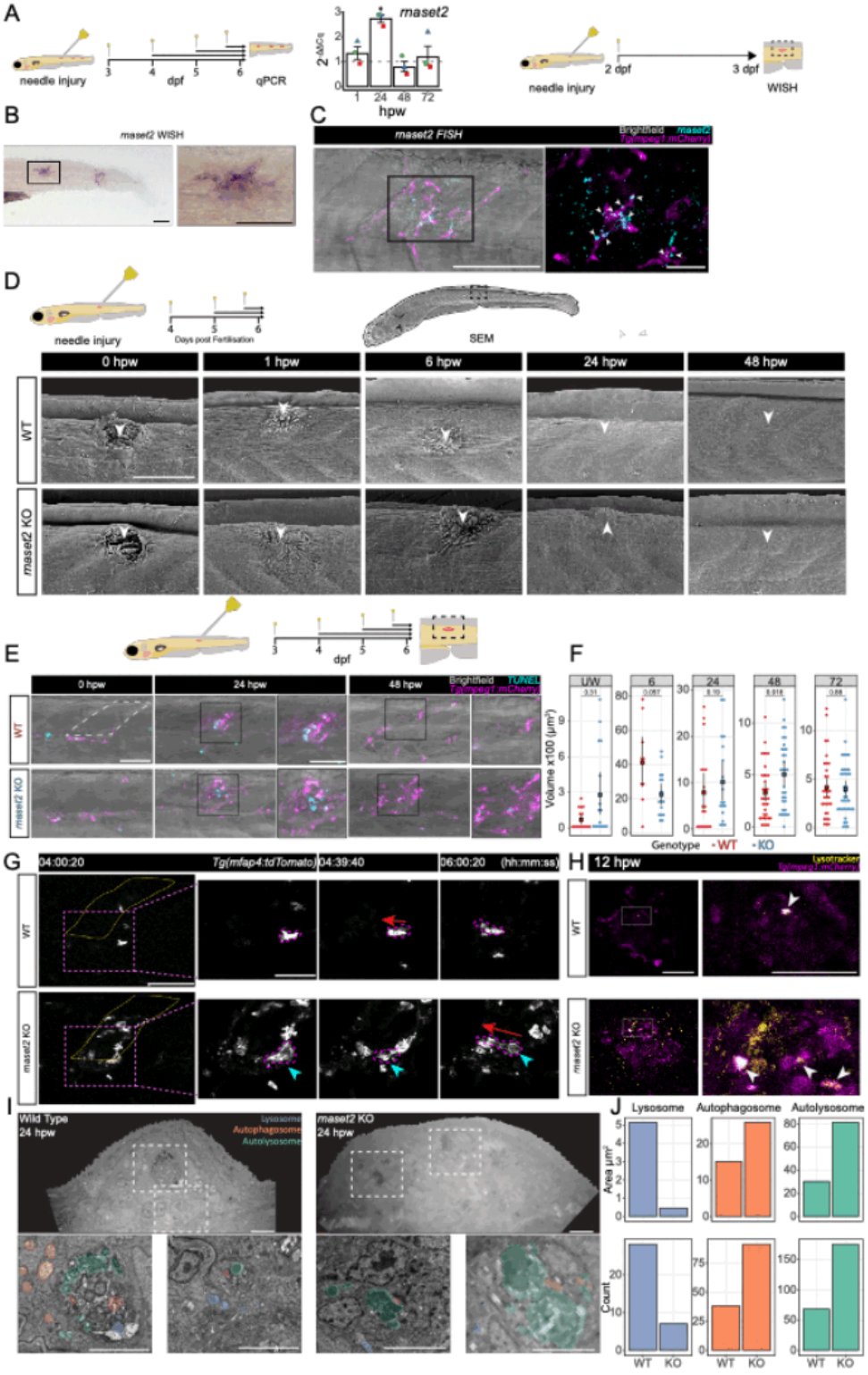


Figure 3

Rnaset2 is induced in wound-associated macrophages and promotes wound resolution in zebrafish.

(A) Experimental timeline for wounding and subsequent qRT-PCR and wholemount *in situ* hybridisation (WISH) analyses. qRT-PCR show increased *rnaset2* expression at 24 h post-wounding (hpw). **(B)** Wound-associated expression of *rnaset2* detected by DIG-labelled WISH in 3 dpf zebrafish larvae at 24 hpw. Higher-magnification image shows *rnaset2* expression surrounding an individual wound. **(C)** Multi-channel confocal brightfield

images of the flank region of 24 hours post wounding 3 dpf *Tg(mpeg:Gal4FF); Tg(UAS:NfsB-mCherry)* transgenic zebrafish larva. Macrophages were visualised by anti-RFP immunostaining (magenta), and *rnaset2* transcripts were detected by fluorescent *in situ* hybridisation using a Cy5-conjugated tyramide signal amplification system (cyan). Higher magnification view denoted by black inset. White arrowheads indicate expression of *rnaset2* in macrophages. **(D)** SEM time course of wound closure in 6 dpf WT and *rnaset2*^{sh532} mutant (KO) larvae at 0 and 48 hpw. Low-magnification images show the wounded flank. White arrowheads indicate the wound site. **(E)** Delayed clearance of apoptosis in *rnaset2*^{sh532} mutant wounds. TUNEL staining of WT and *rnaset2*^{sh532} KO larvae at the indicated times following wounding. Double-stranded DNA breaks are shown in cyan and macrophages in magenta. White dashed boxes indicate representative wound regions; boxed regions are shown at higher magnification. **(F)** Quantification of TUNEL staining in the wound region at each timepoint. Each point represents data from a single larva and the point colour indicates genotype (Red = WT, Blue= KO). Mean values (black square) are plotted with 95% confidence intervals. Data were analysed using unpaired two-sided Mann-Whitney tests. Specimen numbers are n = 16 (WT) and 16 (KO) for unwounded; 9 (WT) and 16 (KO) at 6 hpw; 18 (WT) and 18 (KO) at 24 hpw; 35 (WT) and 32 (KO) at 48 hpw; and 32 (WT) and 38 (KO) at 72 hpw. **(G)** More persistent and more swollen macrophages in *rnaset2*^{sh532} mutant wounds. Time-lapse imaging of macrophages at wound sites in 5 dpf WT and *rnaset2*^{sh532} KO larvae. Yellow region outlines the wounded somite, and pink boxes indicate the region of high magnification images. Cyan arrowheads indicate large inclusions within macrophages. Magenta outline indicates macrophage margins. Red arrow indicates direction of macrophage migration. **(H)** More abundant and swollen lysosomes in *rnaset2*^{sh532} mutant wounds. Multi-channel confocal time lapse images of WT and *rnaset2*^{sh532} KO larvae expressing the macrophage reporter Tg(*mpeg1:mCherryCAAX*) were stained with LysoTracker Green DND-20 to reveal lysosomes (yellow). White arrowheads indicate indicate LysoTracker-positive compartments within macrophages. **(I)** Increased accumulation of late-stage autophagic compartments of macrophages in *rnaset2*^{sh532} mutant zebrafish. Transmission Electron Microscopy (TEM) of transverse sections through the wound region in WT and *rnaset2*^{sh532} KO larvae at 24 hpw. Higher-magnification images corresponding to boxed regions are false coloured to indicate lysosomes (blue), autophagosomes (orange), autolysosomes (green). **(J)** Quantification of the size and number of lysosomes, autophagosomes and autolysosomes in the wound region of WT and *rnaset2*^{sh532} KO larvae. Scale bars: B, C, D, E and G, 100 μm; C inset, 20 μm; E inset, 50 μm; G inset, 25 μm; H, 5 μm.

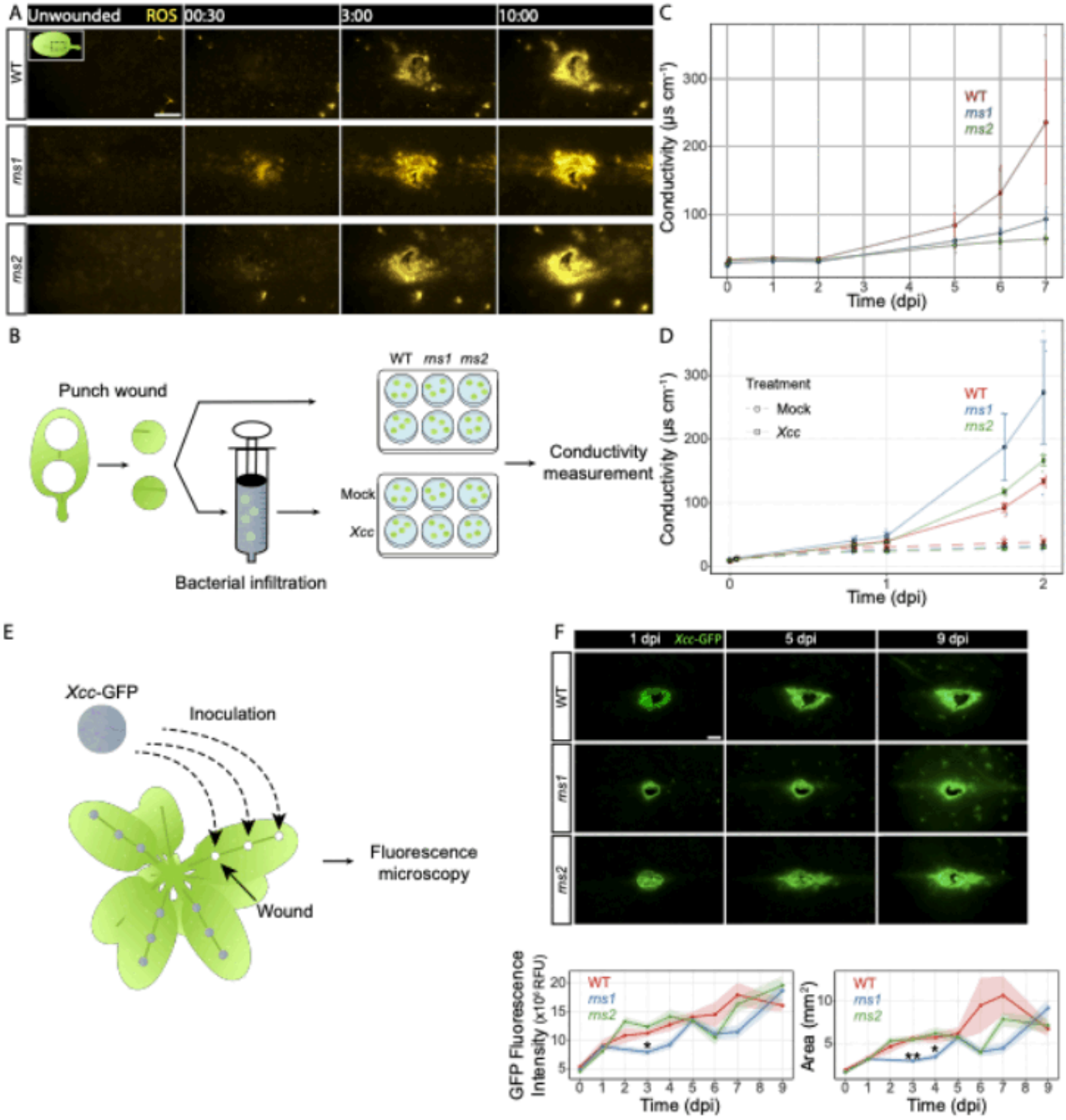


Figure 4

Loss of RNS1 enhances wound-triggered antibacterial defence in Arabidopsis.

(A) Wound-induced oxidative response is accelerated in *rns1*mutants. WT, *rns1* and *rns2* plants were fumigated with 50 µM H_2DCFDA and leaves were mechanically wounded before time-lapse fluorescence imaging. Oxidative response was monitored at the wound site before wounding (unwounded) and at 30 s, 3 min and 10 min post-wounding. **(B)**Experimental procedure for the electrolyte leakage assays. Leaf discs from WT, *rns1*and *rns2* plants were generated by mechanical punching. Electrolyte leakage was monitored by conductivity over time either directly after punching (C) or after vacuum infiltration with 10^8 CFU mL^{-1}

*Xcc*Race6 or water (Mock) (D). **(C)** Wound-associated electrolyte leakage is reduced in *rns1* and *rns2* mutants. Error bars indicate mean ± SE of n = 3 biological replicates. **(D)** Infection-associated electrolyte leakage is increased in *rns1* mutants. Error bars indicate mean ± SE of n = 3 biological replicates. **(E)** Experimental procedure for monitoring bacterial colonization. WT, *rns1* and *rns2* leaves were wounded and inoculated with 10^9 CFU mL^{-1} GFP-expressing *Xcc*Race6. Bacterial colonization was visualized by fluorescence microscopy over time. **(F)**Early wound colonisation by *Xcc*Race6 is reduced in *rns1* mutants. Bacterial colonization was quantified by fluorescence intensity and colonized area. Shaded regions indicate mean ± SE. Specimen numbers are n = 4 (WT) and 4 (*rns1*) for 0 dpi; 6 (WT) and 4 (*rns1*) at 1 dpi; 20 (WT) and 4 (*rns1*) at 3 dpi; 8 (WT) and 4 (*rns1*) at 4 dpi; and 12 (WT) and 12 (*rns1*) at 5 dpi, 4 (WT) and 4 (*rns1*) at 6 dpi, 6 (WT) and 4 (*rns1*) at 7 dpi, 4 (WT) and 4 (*rns1*) at 9 dpi. Unpaired two-sided Mann-Whitney-test was used to determine *P* values, *P < 0.05, **P < 0.01. Scale Bars: A and E = 1 mm

Supplementary Files

This is a list of supplementary files associated with this preprint. Click to download.

- SupplementaryFigure1.pdf
- SupplementaryMovie3.mov
- SupplementaryMovie2.mov
- SupplementaryMovie1.mov
- Onlinefloatimage1.png